Nanoscale

Accepted Manuscript

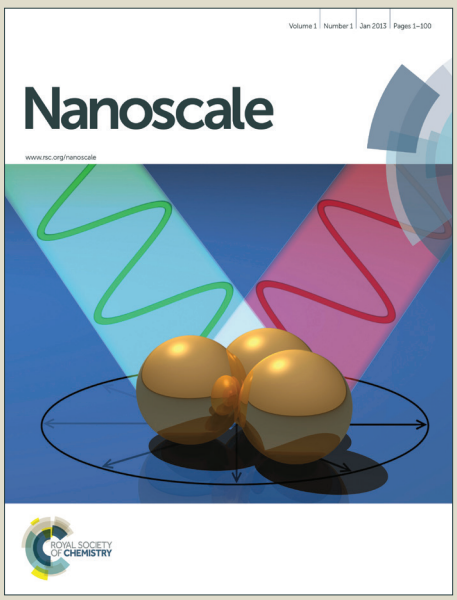

ROYAL SOCIETY OF CHEMISTRY

www.rsc.org/nanoscale

Journal Name

ARTICLE

Two-dimensional transition-metal dichalcogenide alloys: preparation, characterization and applications

Received 00th January 20xx,
Accepted 00th January 20xx

DOI: 10.1039/x0xx00000x

www.rsc.org/

L. M. Xie[a]

Engineering electronic structure of atomically thin two-dimensional (2D) materials is of great importance to their potential applications. In comparison to many other approaches such as strain and chemical functionization, alloying can contineously tune the bandgaps in a wide energy range. Atomically thin 2D alloys have been prepared and studied recently motivated by their potentials in electronic and optoelectronic applications. Here in this review, we first summerize the preparation of 2D alloys (mainly on transition-metal dichalcogenide (TMD) monoalyer alloys), including mechanical exfoliation, physical vapor deposition (PVD), chemical vapor depostion (CVD) and chalcogen exchange. Then atomic-resolution imaging, Raman and photoluminescence (PL) spectroscopic characterization of 2D alloys are reviewed, in which bandgap tuning is discussed in details based on the PL experiments and theoretical calculations. At last, applications of 2D alloys in field-effect transistors (FETs), photocurrent generation and hydrogen evolution catalysis are reviewed.

Introduction

Since the discovery of graphene in 2004[1], atomically thin materials (*i.e.*, two-dimensional (2D) materials) have attracted broad interest[2-8] because of their unique structures and physical properties. Towards potential applications in electronics and optoelectronics, 2D materials with sizable bandgaps and high carrier mobilities are needed[9-11]. Graphene has extremely high carrier mobility[12] (>10^5 cm^2/Vs) but with zero bandgap. Many efforts have been made to open a bandgap in graphene, such as asymmetric grating[13]/doping of bilayer graphene[14], hydrogenation[15]/fluorination[16]/chlorination[17] of graphene. However, so far, the bandgap opening for graphene is either too small or too large (<0.4 eV for asymmetric gating[13] and 3.5-3.7 eV for graphane[18]). Meanwhile, many other 2D materials, especially 2D semiconducting materials, are emerging (Figure 1 and Table 1) and have already shown excellent electronic[2, 19, 20] and optoelectronic properties (such as high power/mass light harvesting[21, 22], extremely-high sensitive photon detection[23] and low-threshold lasing[24]).

The large family of 2D materials includes (1) transition-metal dichalcogenides (TMDs) (such as MoS_2, $MoSe_2$, WS_2, WSe_2, ZrS_2, ReS_2), (2) hexagonal BN (*h*-BN), (3) X-ene (graphene, silicene and germanene), (4) black phosphorus (b-P, *i.e.*, phosphorene), (5) group IIIA chalcogenides (such as GaS, GaSe) and (6) group IVA dichalcogenides (such as SnS_2) and so on.

Fine tuning the bandgap as well as valence band (VB) and conduction band (CB) positions are of great importance to engineer the performance of 2D-material based devices. Alloying different materials (especially semiconductors) offers vast space for tuning the electronic structure as well as the lattice parameters[25]. Bulk semiconductor alloys have been intensively studied[25]. In the last few years, much work has been done on 2D semiconductor alloys (mainly TMD monolayer alloys). In this review, we summarize recent work on 2D semiconductor alloys, including the synthesis, structure characterization, Raman and photoluminescence (PL) spectroscopic properties, electronic structure, and potential applications.

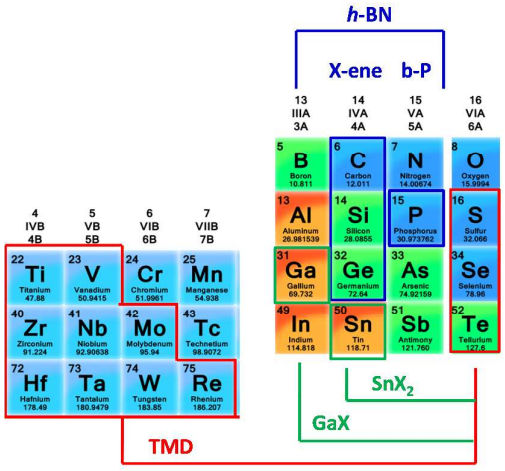

Figure 1. Selected 2D materials in the periodic table.

Choices of the end materials for 2D TMD alloys

Bandgaps of 2D materials ranges from zero to UV region (Figure 2). For example, X-ene, TiX_2 (X= Se and Te), group VB TMDs, WTe_2, $ZrTe_2$ and $HfTe_2$ are metallic[1, 26, 27]. TiS_2 has calculated bandgaps of

[a] *Key Laboratory of Standardization and Measurement for Nanotechnology of Chinese Academy of Sciences, National Center for Nanoscience and Technology, Beijing 100190, P. R. China*

~0.02 eV[27]. $ZrSe_2$ and $HfSe_2$ have a bandgap in the IR range[27]. Other 2D materials (such as GaX, SnX_2, ReX_2, black phosphorus, ZrS_2, HfS_2, group VIB TMDs except WTe_2) have bandgaps in the visible and NIR range[7, 27].

Table 1. Lattice parameters and bandgaps of selected 2D materials

Monolayer material	Lattice parameters (from the bulk material)	Bond lengths (nm)	Band-gap (cal., in eV)	Band-gap (exp., in eV)
Graphene	a=b=0.246nm θ=120°	0.142	0	-
h-BN	a=b=0.250nm θ=120°	0.144	4.7	-
Silicene	a=b=0.387nm θ=120° (Bulking of 0.068 nm)[a]	0.234[a]	0[a]	-
Germanene	a=b=0.406nm θ=120° (Bulking of 0.046 nm)[a]	0.244[a]	0[a]	-
Black phosphorus (Phosphorene)	a=0.331nm b=0.438nm θ=90°[b]	0.222 0.224[b]	2.0[c]	1.3[d]
MoS_2 (2H phase)	a=b=0.315nm θ=120°	0.239	1.6	1.85[e]
$MoSe_2$ (2H phase)	a=b=0.329nm θ=120°	0.249	1.4	1.55[f]
$MoTe_2$ (rt phase)	a=b=0.352nm θ=120°	0.268	1.15	1.1[g]
WS_2	a=b=0.316nm θ=120°	0.240	1.8	1.99[h]
WSe_2	a=b=0.329nm θ=120°	0.250	1.5	1.65[i]
WTe_2	a=0.348nm b=0.626nm θ=90°	0.270 0.271 0.272 0.280 0.281 0.286	0	-
ZrS_2	a=b=0.365nm θ=120°	0.256	1.1	-
$ZrSe_2$	a=b=0.377nm θ=120°	0.266	0.4	-
$ZrTe_2$	a=b=0.395nm θ=120°	0.282	0	-
HfS_2	a=b=0.363nm θ=120°	0.255	1.3	-
$HfSe_2$	a=b=0.379nm θ=120°	0.267	0.6	-
$HfTe_2$	a=b=0.395nm θ=120°	0.291	0	-
ReS_2	a=0.642nm b=0.651nm θ=106.5°	0.234 0.240 0.247 0.250	1.4	1.55[j]
$ReSe_2$	a=0.660nm b=0.672nm θ=118.9°	0.235 0.238 0.260 0.261 0.262	1.3	1.32[k]
SnS_2	a=b=0.365nm θ=120°	0.256	1.6	-
$SnSe_2$	a=b=0.381nm θ=120°	0.268	0.8	-
GaS	a=b=0.359nm θ=120°	0.233	2.6	-
GaSe (2H phase)	a=b=0.374nm θ=120°	0.247	2.3	-
TiS_2	a=b=0.341nm θ=120°	0.243	0.02	-
$TiSe_2$	a=b=0.354nm θ=120°	0.255	0	-
$TiTe_2$	a=b=0.376nm θ=120°	0.277	0	-
NbS_2 (ht phase)	a=b=0.331nm θ=120°	0.242	0	-
$NbSe_2$ (3R phase)	a=b=0.345nm θ=120°	0.261	0	-
TaS_2 (α phase)	a=b=0.335nm θ=120°	0.243	0	-
$TaSe_2$ (1T phase)	a=b=0.351nm θ=120°	0.256	0	-
$TaTe_2$ (mon phase)	a=b=0.364nm θ=120°	0.268	0	-

Note: All unspecified lattice parameters and bond lengths are from www.springermaterials.com. All unspecified bandgaps are from ref. [27]. In cases of multi-phases for the corresponding bulk materials, lattice parameters for a certain phase are shown in the table.
[a]ref.[26]; [b]ref.[28]; [c]ref.[29]; [d]ref.[30]; [e]ref.[6]; [f]ref.[31, 32]; [g]ref. [33]; [h]ref.[34]; [i]ref.[31]; [j]ref.[35]; [k]ref. [36].

Graphene and *h*-BN have a similar crystal structure with only ~1.5% lattice mismatch. Theoretical calculations have predicted that hexagonal ordered and disordered BCN can have a sizable bandgap[37-39]. However, graphene and *h*-BN are not soluble in each other and, so far, BCN films with separated BN and graphene domains have been obtained[40].

For most TMDs, depending on *d* orbital filling, transition-metal atoms can be coordinated by six chalcogen atoms in a configuration of triangular prism (for example, 2H-MoS_2), octahedron (for example, ZrS_2) or distorted octahedron (for example, ReS_2). From the structure point, alloying TMDs within the same transition group is usually feasible because of same lattice symmetry as well as small lattice mismatches. For example, MoX_2 and WX_2 (X=S, Se and Te), ZrX_2 and HfX_2 (X=S and Se) have lattice mismatches less than 1% (Table 1 and Figure 2a). Alloying TMDs between different transition groups is rather challenging because of possibly different chalcogen coordination configurations and larger lattice mismatches. For example, MoX_2 and ZrX_2 (X=S, Se and Te) have chalcogen coordinations of triangular prism and octahedron, respectively, and a lattice mismatch of ~5-7% (Table 1 and Figure 2a). In case of alloying materials with different crystal structures, the bond lengths (Figure 2b) can be used to estimate the lattice mismatches.

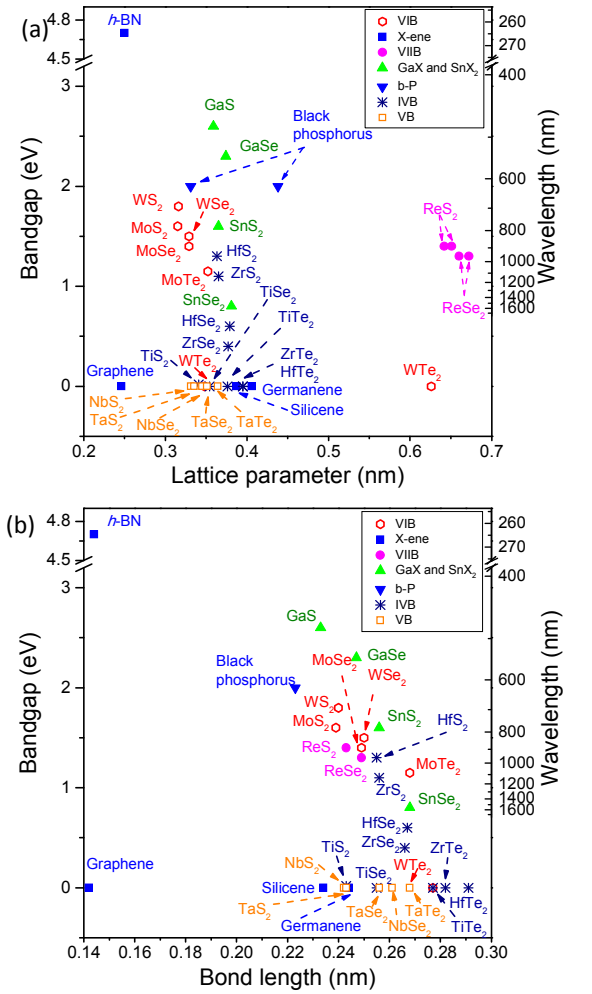

Figure 2. Plots of (a) calculated bandgaps against lattice parameters and (b) calculated bandgaps against bond lengths for selected 2D materials. Note: the corresponding numeral data and references are in Table 1. In panel a, both lattice parameters *a* and *b* are shown for black phosphorus, WTe_2, ReS_2 and $ReSe_2$. In panel b, average bond lengths for black phosphorus, WTe_2, ReS_2 and $ReSe_2$ are used.

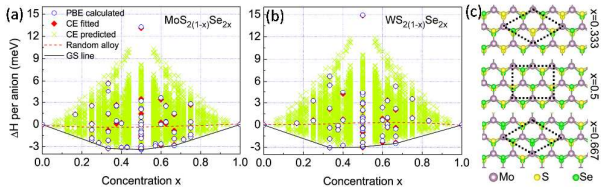

Figure 3. Calculated formation enthalpies for (a) $MoS_{2(1-x)}Se_{2x}$ and (b) $WS_{2(1-x)}Se_{2x}$ monolayers. (c) Structures of ordered $MoS_{2(1-x)}Se_{2x}$ monolayers. Reproduced with permission from ref. [41]. Copyright 2013, AIP Publishing LLC.

Many TMD bulk alloys were synthesized in the last century, such as $Mo_{1-x}W_xS_2$[42], $Mo_{1-x}W_xSe_2$[43], $TaS_{2(1-x)}Se_{2x}$[44], $ZrS_{2(1-x)}Se_{2x}$[45], $HfS_{2(1-x)}Se_{2x}$[46] and $ReS_{2(1-x)}Se_{2x}$[47]. For TMD monolayer alloys, theoretical calculations have shown that ordered phases have a lower energy of a few meV than the random phases[41, 48] (Figure 3). Since synthesis of TMD monolayer alloys is usually done at high temperatures of a few hundreds of degrees, the random phases are more preferred due to the large entropy. So far $MoS_{2(1-x)}Se_{2x}$[49-54], $WS_{2(1-x)}Se_{2x}$[55], $Mo_{1-x}W_xS_2$[34, 56, 57], $Mo_{1-x}W_xSe_2$[31, 58] monolayers with random structures have been obtained.

Synthesis of 2D TMD alloys

Mechanical exfoliation of bulk alloys

All reported TMD bulk alloys can be mechanically exfoliated into monolayers. The first exfoliated TMD monolayers alloy are $Mo_{1-x}W_xS_2$ monolayers[34] (Figure 4). The composition of $Mo_{1-x}W_xS_2$ bulk alloys was tuned by changing the loading ratio of MoS_2 and $MoSe_2$ powders in the chemical vapor transport (CVT) synthesis. After mechanical exfoliation, $Mo_{1-x}W_xS_2$ monolayers show a red contrast of ~10% under optical microscope, which can be used to discriminate and locate the monolayers. AFM imaging can be used to confirm the monolayer thickness (~0.7nm). $Mo_{1-x}W_xSe_2$ monolayers have also been prepared by mechanical exfoliation[31, 58].

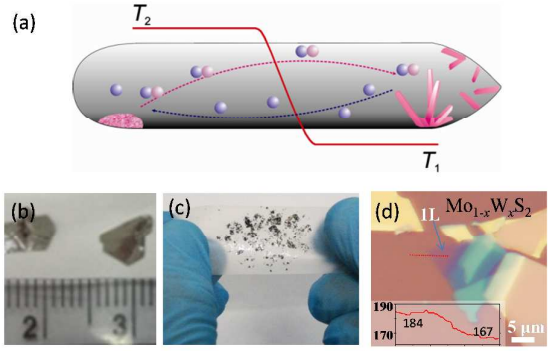

Figure 4. (a) Illustration of CVT method (Reproduced with permission from ref. [59]). Optical images of (b) single crystals of TMD bulk alloys and (c) exfoliated TMD alloy flakes on a tape. (d) Optical image of a $Mo_{1-x}W_xS_2$ monolayer flake on SiO_2/Si (oxide thickness of 300 nm). Panel b and d are reproduced with permission from ref. [31] and ref. [34], respectively. Copyright © American Chemical Society.

Physical vapor deposition (PVD)

For end materials such as MoS_2 and $MoSe_2$, which have significant vapor pressures at moderate growth temperatures, the corresponding monolayer alloys can be prepared by direct vaporization of the powders of the end materials and then deposition on substrates at a lower temperature (Figure 5). In the PVD synthesis of $MoS_{2(1-x)}Se_{2x}$ monolayers, continuous films and large triangle domains (~20 μm) can be obtained[52, 53], in which the system pressure, H_2 flow rate, deposition temperature, deposition temperature gradient and growth time play key roles in the synthesis. The composition of $MoS_{2(1-x)}Se_{2x}$ can be controlled by changing the evaporation temperatures of MoS_2 and $MoSe_2$ powders.

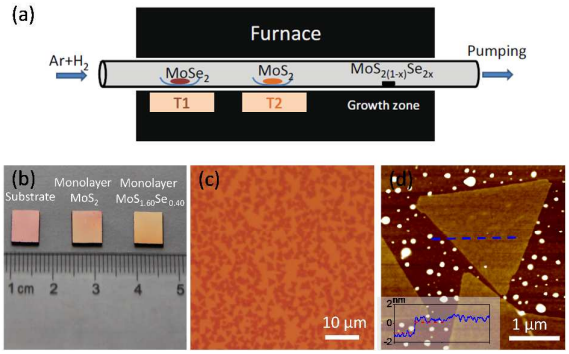

Figure 5. (a) Illustration of three-zone low-pressure furnace system for PVD synthesis of $MoS_{2(1-x)}Se_{2x}$ monolayers. (b) Optical image of as-grown $MoS_{2(1-x)}Se_{2x}$ films on SiO_2/Si substrates. (c) Optical image and (d) AFM image of $MoS_{2(1-x)}Se_{2x}$ monolayers. Reproduced with permission from ref. [53]. Copyright 2014, John Wiley and Sons.

Chemical vapor deposition (CVD)

The widely used approach for synthesis of TMD monolayer alloys is sulfurization and selenization of transition-metal oxides (such as MoO_3 and WO_3)[49-51, 54, 57, 60, 61]. The evaporation temperatures of S and Se were tuned to control the S and Se vapor pressures and hence control S/Se ratio in the as-prepared $MoS_{2(1-x)}Se_{2x}$ monolayers (Figure 6). The reaction was usually done at ~700 °C. Additionally, sulfurization and selenization of transition metals (such as Mo and W)[62] can also be used to prepare the corresponding 2D alloys.

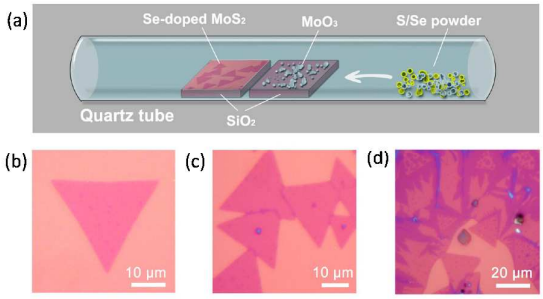

Figure 6. (a) Illustration of synthesis of $MoS_{2(1-x)}Se_{2x}$ monolayers using MoO_3 and S/Se as precursors. (b)-(d) Optical images of as-prepared $MoS_{2(1-x)}Se_{2x}$ monolayers. Reproduced with permission from ref. [50]. Copyright © American Chemical Society.

For ZrX_2 (X=S, Se) synthesis, $ZrCl_4$ can be used as a precursor. Further, *h*-BN template is needed to grow ZrX_2 monolayers on substrates[63]. By using both S and Se as precursors and changing the S/Se evaporation temperatures, $ZrS_{2(1-x)}Se_{2x}$ monolayer alloys can also be synthesized (unpublished data).

Chalcogen exchange

At high temperatures, chalcogen atoms in TMD monolayers can be replaced by hetero-chalcogen atoms[64, 65]. For example, S atoms in MoS_2 monolayers can be replaced by Se atoms at a temperature of 700-900 °C and then $MoS_{2(1-x)}Se_{2x}$ monolayers can be obtained.

Preparation of 2D-alloy based hetero-structures

In the CVD synthesis of $MoS_{2(1-x)}Se_{2x}$ monolayers, lateral hetero-structures can be prepared by changing the S/Se ratio during the deposition[60]. In the experiments, the evaporation temperatures of S and Se changed continuously and $MoS_{2(1-x)}Se_{2x}$ monolayers with increasing Se content from the center to edges were obtained (Figure 7a).

2D-alloy based vertical hetero-structures can also be prepared[57]. Atomic layer deposition (ALD) is used to prepared $WO_y/Mo_{1-x}W_xO_y/MoO_y$ vertical structure and then followed by sulfurization to form $MoS_2/Mo_{1-x}W_xS_2/WS_2$ vertical hetero-structure (Figure 7b). This vertical hetero-structure has shown promising photoelectrical response.

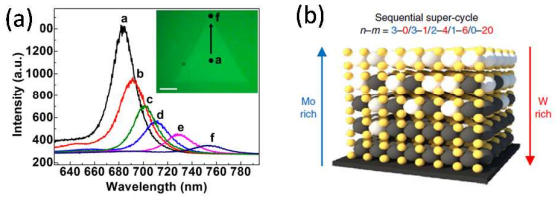

Figure 7. (a) CVD-grown $MoS_{2(1-x)}Se_{2x}$ lateral hetero-structure with continuous Se gradient from the center to the edge. Reproduced with permission from ref. [60]. Copyright © American Chemical Society. (b) Structure illustration of prepared $MoS_2/Mo_{1-x}W_xS_2/WS_2$ vertical hetero-structure. Reproduced with permission from ref. [57]. Copyright 2015, Nature Publishing Group.

Characterization of 2D TMD alloys

Scanning transmission electron microscopic (STEM) imaging

Atom arrangement in 2D TMD alloys (i.e., ordered, disordered or clustered) determines the electronic structure. One direct way to image the atom arrangement is to use high-angle-annual-dark-field (HAADF) STEM imaging which has atomic resolution and Z-contrast capability (contrast proportional to ~ $Z^{1.4\text{-}1.6}$)[66]. HAADF STEM imaging has been conducted on $Mo_{1-x}W_xS_2$[34, 57, 67], $MoS_{2(1-x)}Se_{2x}$[50, 53] and $WS_{2(1-x)}Se_{2x}$ monolayers[55].

Since Mo and W have different atomic numbers (46 and 56, respectively), HAADF STEM can discriminate individual Mo and W atoms in $Mo_{1-x}W_xS_2$ monolayers (Figure 8a,b). Calculation of short range order parameters by counting average Mo atoms around W atoms revealed random distributions of Mo and W atoms in $Mo_{1-x}W_xS_2$ monolayers[34, 67].

For $MoS_{2(1-x)}Se_{2x}$ monolayers, Mo sites should have a similar HAADF STEM contrast while X_2 sites should have different STEM contrasts because of several possible atom combinations (S_2, SSe and Se_2) for the X_2 sites. Experimental results[53] have shown that S_2, SSe and Se_2 sites can be discriminated by quantitative analysis of STEM intensity (Figure 8c,d). Different coordinations of X_2 around Mo atoms have

been observed (white triangles in Figure 8d). Distribution of the different X_2 configurations matches well with the binominal distribution calculated from the Se content (Figure 8e), indicating random distributions of S and Se atoms.

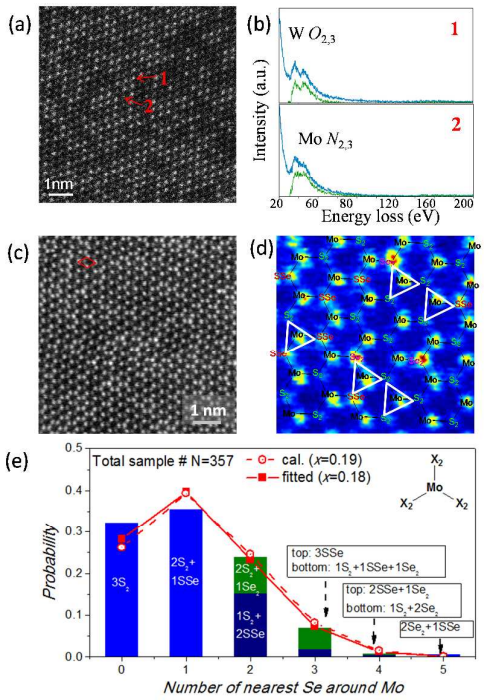

Figure 8. (a) HAADF STEM image of a $Mo_{1-x}W_xS_2$ monolayer and (b) electron energy loss spectra (EELS) from two individual atoms assigned to W and Mo atoms. Reproduced with permission from ref. [34]. Copyright © American Chemical Society. (c) HAADF STEM image of a $MoS_{2(1-x)}Se_{2x}$ monolayer, (d) the structure schematic and (e) the coordination statistics. Reproduced with permission from ref. [53]. Copyright 2014, John Wiley and Sons.

PL spectroscopic characterization

Group VIB TMD monolayers have direct bandgaps and the corresponding monolayer alloys are also direct bandgap semiconductors with strong PL emissions. As the composition changes, group VIB TMD monolayer alloys show continuous shift of PL emission wavelengths (Figure 9). For example, the emission wavelengths of $MoS_{2(1-x)}Se_{2x}$ [49-53], $Mo_{1-x}W_xS_2$ [34] and $Mo_{1-x}W_xSe_2$ [31, 58] monolayers can be continuously tuned in the range of 670-800 nm, 620-680 nm and 760-780 nm, respectively. Note that the shoulder emission at higher energy side (called B exciton emission) and the main peak (called A exciton emission) are due to spin-orbit splitting of VB at the K point[6].

Emission energy against composition for $MoS_{2(1-x)}Se_{2x}$, $Mo_{1-x}W_xS_2$, $Mo_{1-x}W_xSe_2$ and $WS_{2(1-x)}Se_{2x}$ monolayers is plotted in Figure 10. The emission energy shows a bowing as the composition changes, which is called bandgap bowing[25]. Bandgap bowing can be described by quadratic equation

$$E_{g,A_{1-x}B_xX_2} = (1-x)E_{g,AX_2} + xE_{g,BX_2} - bx(1-x) \quad (1)$$

where $E_{g,A_{1-x}B_xX_2}$, E_{g,AX_2} and E_{g,BX_2} are the bandgaps of the alloy and the corresponding end materials, *b* is the bowing parameter.

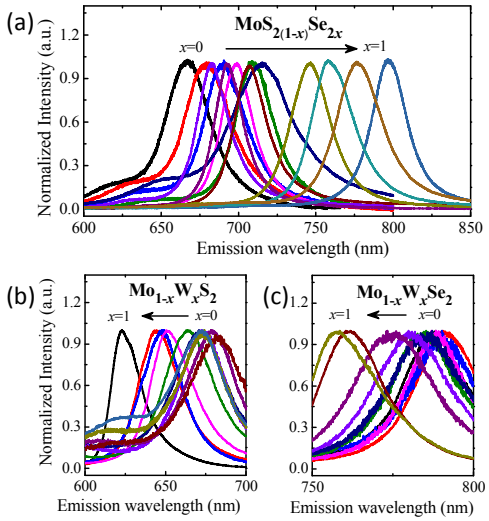

Figure 9. Composition-dependent PL spectra of (a) $MoS_{2(1-x)}Se_{2x}$ monolayers, (b) $Mo_{1-x}W_xS_2$ monolayers and (c) $Mo_{1-x}W_xSe_2$ monolayers in the whole composition range (*x*=0-1). Data are adopted from refs. [31, 34, 52, 53] and replotted.

$Mo_{1-x}W_xS_2$ monolayer shows a large bandgap bowing (*b*=0.25 eV[34]) compared to the bulk material (*b*~0.05 eV[42]), which results in a minimum emission energy reached at *x*=0.2-0.3 for $Mo_{1-x}W_xS_2$ monolayer. While $MoS_{2(1-x)}Se_{2x}$ monolayer has a small bandgap bowing (*b*~0.05 eV[52]). The origin of bandgap bowing can be lattice mismatch, orbital hybridization and so on[68]. For $Mo_{1-x}W_xS_2$ monolayers, density functional theory (DFT) calculation have shown that the bowing is from the lowest unoccupied molecular orbital (LUMO), which is due to different LUMO compositions for MoS_2 and WS_2 monolayers[34].

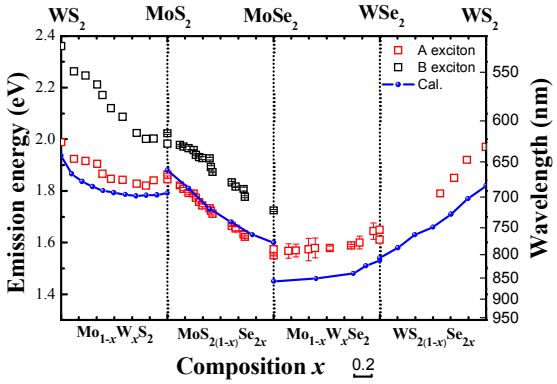

Figure 10. Composition-dependent experimental and calculated emission energies (in eV and nm) for $Mo_{1-x}W_xS_2$, $MoS_{2(1-x)}Se_{2x}$, $Mo_{1-x}W_xSe_2$ and $WS_{2(1-x)}Se_{2x}$ monolayers. Experimental data are adopted from refs. [31, 34, 52, 53, 55]. Calculated data are adopted from refs.[34, 41, 69].

Raman spectroscopic characterization

Raman spectroscopy is a sensitive, non-destructive and convenient tool to characterize structures of alloys. There are one-mode behavior and two-mode behavior for different Raman modes in the alloys[70]. For one-mode behavior, the same Raman modes in the two end materials merge into one branch as the composition changes. For two-mode behavior, the Raman modes with same symmetry in the two end materials show two different branches instead of merging into one branch. Many models have been proposed to explain Raman behaviors in alloys, including clustering[71], spatial correlation[72] and random element isodisplacement (REI)[70].

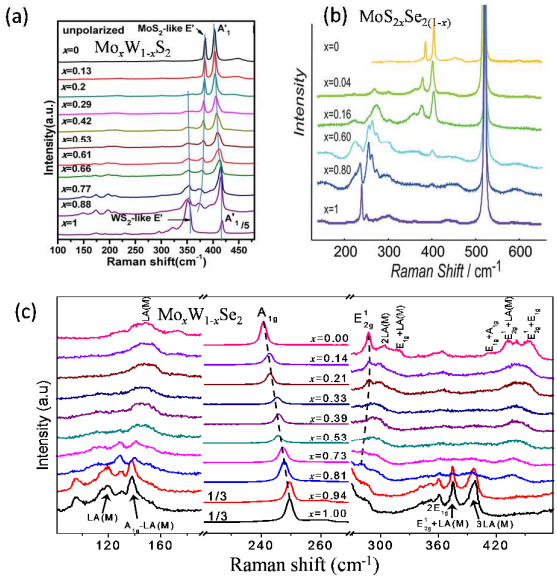

Figure 11. Composition-dependent Raman spectra of (a) $Mo_{1-x}W_xS_2$ monolayers, (b) $MoS_{2(1-x)}Se_{2x}$ monolayers and (c) $Mo_{1-x}W_xSe_2$ monolayers. Panel a is reproduced with permission from ref. [73] Copyright 2014, the Royal Society of Chemistry. Panel b is reproduced with permission from ref. [49]. Copyright 2014, John Wiley and Sons. Panel c is reproduced with permission from ref.[31]. Copyright © American Chemical Society.

Modified REI (MREI)[74] is based on two assumptions: one is random arrangement of alloy elements and the other is same vibrational phase and amplitude for the same kind of atoms. MREI can be well applied to 2D alloys. In $Mo_{1-x}W_xS_2$ and $Mo_{1-x}W_xSe_2$ monolayers, A'_1 mode (corresponding to A_{1g} mode in the bulk materials) showed one-mode behavior and E' mode (corresponding to $E_{2g}{}^1$ mode in the bulk materials) showed two-mode behavior (Figure 11a,c)[31, 73]. All second-order Raman modes in $Mo_{1-x}W_xS_2$ and $Mo_{1-x}W_xSe_2$ monolayers showed two-mode behavior (Figure 11a,c). The composition-dependent A'_1 and E' frequencies can be well fitted by MREI model, yielding force parameters and composition depending frequency shift. For $Mo_{1-x}W_xS_2$ monolayers[73],

$$\omega_{A'_1} = 401.6(1 + 0.080x + 0.002x^2)^{1/2} \quad (2)$$

and for $Mo_{1-x}W_xSe_2$ monolayers[31],

$$\omega_{A'_1} = 204.1(1 + 0.057x - 0.023x^2)^{1/2} \quad (3)$$

The composition-dependent Raman shift can be used to quantify alloy compositions.

For $MoS_{2(1-x)}Se_{2x}$ monolayers, both A'_1 and E' modes showed two-mode behavior (Figure 11b)[49]. Splitting of A'_1 mode has also been observed, which is assigned to the different S/Se configurations around Mo atoms[75].

Applications of 2D TMD alloys

Field-effect transistors (FETs)

FETs with high on/off ratios are expected for semiconducting 2D alloys. For $Mo_{1-x}W_xSe_2$ and $MoS_{2(1-x)}Se_{2x}$ monolayers, n-type devices with 10^6 on/off ratio have been obtained (Figure 12). The on-current (at V_{ds}=1 V) is around 0.1-1 μA/μm for back-gate devices. As the composition changes, the positions of VB and CB change[41]. So the shift of onset gate voltage is also expected. At the composition of around 0.3 for $MoS_{2(1-x)}Se_{2x}$ monolayers, ambipolar transport has been observed (Figure 12c).

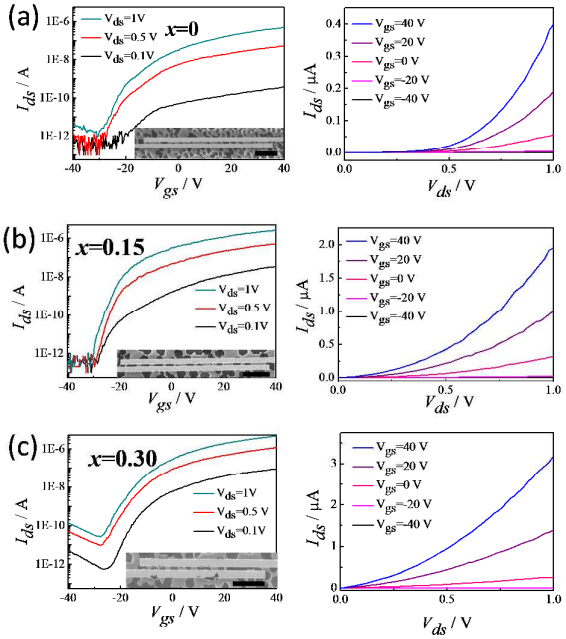

Figure 12. Electrical measurements of FETs fabricated on CVD-grown $MoS_{2(1-x)}Se_{2x}$ monolayers. Reproduced with permission from ref. [53]. Copyright 2014, John Wiley and Sons.

Carrier scattering is expected in 2D alloys considering different electron potentials for different alloying atoms. Additionally, calculations have shown that the effective mass of electrons in $Mo_{1-x}W_xS_2$ alloys is slightly heavier than that in MoS_2 and WS_2 monolayers[76]. So far, limited work has been done on electrical transport of 2D alloys. One experimental result has shown that field-effect mobility is around 0.1-1 cm^2/Vs for $MoS_{2(1-x)}Se_{2x}$ monolayers, at the same level as CVD-grown MoS_2 monolayers[77].

Optoelectronic devices

MoS_2 monolayer based photodetecting devices have already shown high sensitivity up to 800 A/W and response time of a few seconds[23]. TMD monolayer alloys can also have the same potential for high photodetecting sensitivity. In addition, TMD monolayer alloys with tunable bandgaps can offer arbitrary cut-off detection wavelength in visible and NIR region. So far, one work on photon detection using $MoS_{2(1-x)}Se_{2x}$ monolayer alloys[78] has revealed superlinear photocurrent generation with increasing the illumination power.

Recent study has also shown that atomically thick 2D semiconductors can have ultralow lasing threshold[24]. 2D semiconductor alloys hold the potential for micro-lasers in the visible and NIR ranges.

Hydrogen evolution catalysis

Hydrogen evolution reaction (HER) desires a catalyst with H_2 adsorption free energy near zero[79]. Pt is so far the best HER catalyst. MoS_2 also has high HER activity. Alloying of MoS_2 with other materials (such as $MoSe_2$, WS_2) offers the possibility to engineer H_2 affinity and hence improve the HER performance[54, 55, 80, 81]. $MoS_{2(1-x)}Se_{2x}$ few layers have shown a better HER performance, such as an over potential reduce of 50-60 mV compared to MoS_2 and a Tafei slop of 45-55 mV (close to the theoretical value of 40 mV/dec)[80]. $WS_{2(1-x)}Se_{2x}$ (x=0.43) monolayers also have shown an over potential of 80 mV and a Tafei slope of 85 mV/dec, which is significantly lower than WS_2 and WSe_2 monolayers (over potential of 100 and 150 mV, Tafei slopes of 100 mV/dec and 95 mV/dec, respectively, Figure 13)[55].

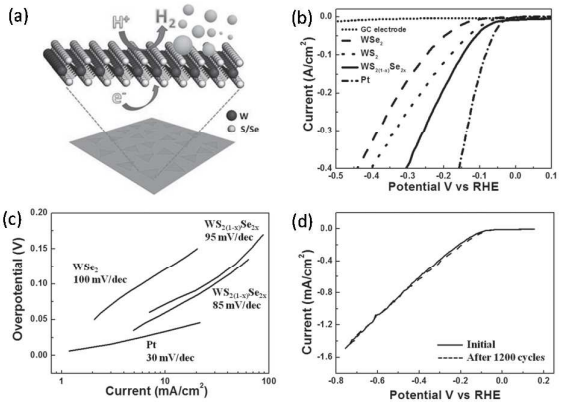

Figure 13. HER performance of $WS_{2(1-x)}Se_{2x}$ monolayers. Reproduced with permission from ref. [55]. Copyright 2015, John Wiley and Sons.

Other 2D semiconductor alloys

Recently, layered black AsP with a similar structure as black phosphorus has been reported (Figure 14)[82]. The bandgap of black AsP few-layers can be tuned from 0.15-0.35 eV (wavelength of around 3.5-8.2 μm), which is suitable for IR detection. IR adsorption experiments show that black AsP have a large anisotropic adsorption in the IR range. The FETs on black AsP have shown a current density up to 0.1 μA/μm and an on/off ratio larger than 10^3.

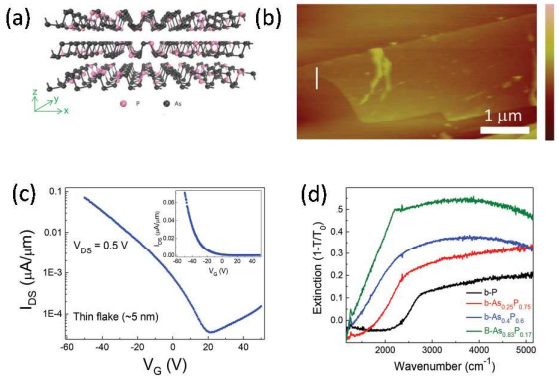

Figure 14. (a) Structure, (b) AFM image, (c) FET performance and (d) IR extinction of balck AsP few-layers. Reproduced with permission from ref. [82] . Copyright 2015, John Wiley and Sons.

Conclusions

Though there are many publications on 2D alloys, the challenge remains. The first challenge is the structure control (ordered or random) in material synthesis, in which thermodynamics and kinetics need be considered. The second challenge is structure characterization. Currently, STEM is a direct tool but it is time-consuming. Another challenge is the stability of 2D materials. 2D materials are usually more reactive than the corresponding bulk materials. For example, silicene, black phosphorus, TiS_2, $HfSe_2$ and even $MoSe_2$ are not stable in air. Then the related alloys may be unstable in air.

At last, current 2D semiconducting alloys are mainly on group VIB TMD monolayer alloys. Further exploring alloys between different groups of TMDs with different *d* electrons is promising for electronic structure engineering beyond bandgap engineering, which can lead to doping, metal-insulator transition (MIT) and so on. Besides TMD alloys, alloys from other 2D materials, such as black AsP and ordered BCN compound, offers the possibility for high-mobility semiconducting materials.

Acknowledgements

L.X. acknowledges support from NSFC (Nos. 21373066, 11304052), Beijing Nova program (No. 2015B049) and partial support from "Strategic Priority Research Program" of the Chinese Academy of Sciences (No. XDA09040300).

Notes and references

1 K. S. Novoselov, A. K. Geim, S. V. Morozov, D. Jiang, Y. Zhang, S. V. Dubonos, I. V. Grigorieva and A. A. Firsov, *Science*, 2004, **306**, 666-669.

2 B. Radisavljevic, A. Radenovic, J. Brivio, V. Giacometti and A. Kis, *Nat. Nanotechnol.*, 2011, **6**, 147-150.

3 M. Derivaz, D. Dentel, R. Stephan, M. C. Hanf, A. Mehdaoui, P. Sonnet and C. Pirri, *Nano Lett.*, 2015, **15**, 2510-2516.
4 B. J. Feng, Z. J. Ding, S. Meng, Y. G. Yao, X. Y. He, P. Cheng, L. Chen and K. H. Wu, *Nano Lett.*, 2012, **12**, 3507-3511.
5 T. Cao, G. Wang, W. P. Han, H. Q. Ye, C. R. Zhu, J. R. Shi, Q. Niu, P. H. Tan, E. Wang, B. L. Liu and J. Feng, *Nat. Commun.*, 2012, **3**, 887.
6 K. F. Mak, C. Lee, J. Hone, J. Shan and T. F. Heinz, *Phys. Rev. Lett.*, 2010, **105**, 136805.
7 L. K. Li, Y. J. Yu, G. J. Ye, Q. Q. Ge, X. D. Ou, H. Wu, D. L. Feng, X. H. Chen and Y. B. Zhang, *Nat. Nanotechnol.*, 2014, **9**, 372-377.
8 C. H. Zhang, L. Fu, S. L. Zhao, Y. Zhou, H. L. Peng and Z. F. Liu, *Adv. Mater.*, 2014, **26**, 1776-1781.
9 G. Fiori, F. Bonaccorso, G. Iannaccone, T. Palacios, D. Neumaier, A. Seabaugh, S. K. Banerjee and L. Colombo, *Nat. Nanotechnol.*, 2014, **9**, 768-779.
10 F. H. L. Koppens, T. Mueller, P. Avouris, A. C. Ferrari, M. S. Vitiello and M. Polini, *Nat. Nanotechnol.*, 2014, **9**, 780-793.
11 F. Schwierz, J. Pezoldt and R. Granzner, *Nanoscale*, 2015, **7**, 8261-8283.
12 C. R. Dean, A. F. Young, I. Meric, C. Lee, L. Wang, S. Sorgenfrei, K. Watanabe, T. Taniguchi, P. Kim, K. L. Shepard and J. Hone, *Nat. Nanotechnol.*, 2010, **5**, 722-726.
13 Y. B. Zhang, T. T. Tang, C. Girit, Z. Hao, M. C. Martin, A. Zettl, M. F. Crommie, Y. R. Shen and F. Wang, *Nature*, 2009, **459**, 820-823.
14 W. J. Zhang, C. T. Lin, K. K. Liu, T. Tite, C. Y. Su, C. H. Chang, Y. H. Lee, C. W. Chu, K. H. Wei, J. L. Kuo and L. J. Li, *ACS Nano*, 2011, **5**, 7517-7524.
15 D. C. Elias, R. R. Nair, T. M. G. Mohiuddin, S. V. Morozov, P. Blake, M. P. Halsall, A. C. Ferrari, D. W. Boukhvalov, M. I. Katsnelson, A. K. Geim and K. S. Novoselov, *Science*, 2009, **323**, 610-613.
16 J. T. Robinson, J. S. Burgess, C. E. Junkermeier, S. C. Badescu, T. L. Reinecke, F. K. Perkins, M. K. Zalalutdniov, J. W. Baldwin, J. C. Culbertson, P. E. Sheehan and E. S. Snow, *Nano Lett.*, 2010, **10**, 3001-3005.
17 J. Wu, L. M. Xie, Y. G. Li, H. L. Wang, Y. J. Ouyang, J. Guo and H. J. Dai, *J. Am. Chem. Soc.*, 2011, **133**, 19668-19671.
18 J. O. Sofo, A. S. Chaudhari and G. D. Barber, *Phys. Rev. B*, 2007, **75**, 153401.
19 H. Wang, L. L. Yu, Y. H. Lee, Y. M. Shi, A. Hsu, M. L. Chin, L. J. Li, M. Dubey, J. Kong and T. Palacios, *Nano Lett.*, 2012, **12**, 4674-4680.
20 K. Kang, S. E. Xie, L. J. Huang, Y. M. Han, P. Y. Huang, K. F. Mak, C. J. Kim, D. Muller and J. Park, *Nature*, 2015, **520**, 656-660.
21 L. Britnell, R. M. Ribeiro, A. Eckmann, R. Jalil, B. D. Belle, A. Mishchenko, Y. J. Kim, R. V. Gorbachev, T. Georgiou, S. V. Morozov, A. N. Grigorenko, A. K. Geim, C. Casiraghi, A. H. Castro Neto and K. S. Novoselov, *Science*, 2013, **340**, 1311-1314.
22 M. Bernardi, M. Palummo and J. C. Grossman, *Nano Lett.*, 2013, **13**, 3664-3670.
23 O. Lopez-Sanchez, D. Lembke, M. Kayci, A. Radenovic and A. Kis, *Nat. Nanotechnol.*, 2013, **8**, 497-501.
24 S. F. Wu, S. Buckley, J. R. Schaibley, L. F. Feng, J. Q. Yan, D. G. Mandrus, F. Hatami, W. Yao, J. Vuckovic, A. Majumdar and X. D. Xu, *Nature*, 2015, **520**, 69-72.
25 S. Adachi, *Properties of Semiconductor Alloys: Group-IV, III-V and II-VI Semiconductors*, Wiley, Chichester, 2009.
26 Z. Y. Ni, Q. H. Liu, K. C. Tang, J. X. Zheng, J. Zhou, R. Qin, Z. X. Gao, D. P. Yu and J. Lu, *Nano Lett.*, 2012, **12**, 113-118.
27 S. Lebegue, T. Bjorkman, M. Klintenberg, R. M. Nieminen and O. Eriksson, *Phys. Rev. X*, 2013, **3**, 031002.
28 H. Asahina and A. Morita, *J. Phys. C Solid State*, 1984, **17**, 1839-1852.
29 Y. Takao and A. Morita, *Physica B & C*, 1981, **105**, 93-98.
30 X. M. Wang, A. M. Jones, K. L. Seyler, V. Tran, Y. C. Jia, H. Zhao, H. Wang, L. Yang, X. D. Xu and F. N. Xia, *Nat. Nanotechnol.*, 2015, **10**, 517-521.
31 M. Zhang, J. X. Wu, Y. M. Zhu, D. O. Dumcenco, J. H. Hong, N. N. Mao, S. B. Deng, Y. F. Chen, Y. L. Yang, C. H. Jin, S. H. Chaki, Y. S. Huang, J. Zhang and L. M. Xie, *ACS Nano*, 2014, **8**, 7130-7137.
32 S. Tongay, J. Zhou, C. Ataca, K. Lo, T. S. Matthews, J. B. Li, J. C. Grossman and J. Q. Wu, *Nano Lett.*, 2012, **12**, 5576-5580.
33 C. Ruppert, O. B. Aslan and T. F. Heinz, *Nano Lett.*, 2014, **14**, 6231-6236.
34 Y. F. Chen, J. Y. Xi, D. O. Dumcenco, Z. Liu, K. Suenaga, D. Wang, Z. G. Shuai, Y.-S. Huang and L. M. Xie, *ACS Nano*, 2013, **7**, 4610-4616.
35 S. Tongay, H. Sahin, C. Ko, A. Luce, W. Fan, K. Liu, J. Zhou, Y. S. Huang, C. H. Ho, J. Y. Yan, D. F. Ogletree, S. Aloni, J. Ji, S. S. Li, J. B. Li, F. M. Peeters and J. Q. Wu, *Nat. Commun.*, 2014, **5**, 4252.
36 H. Zhao, J. B. Wu, H. X. Zhong, Q. S. Guo, X. M. Wang, F. N. Xia, L. Yang, P. H. Tan and H. Wang, *Nano Res.*, 2015, DOI: 10.1007/s12274-12015-10865-12270.
37 Q. Peng, A. Zamiri and S. De, *arXiv:1105.3776v1 [cond-mat.mtrl-sci]*, 2011.
38 X. Blase, A. Rubio, S. G. Louie and M. L. Cohen, *Phys. Rev. B*, 1995, **51**, 6868-6875.
39 A. Y. Liu, R. M. Wentzcovitch and M. L. Cohen, *Phys. Rev. B*, 1989, **39**, 1760-1765.
40 L. Ci, L. Song, C. H. Jin, D. Jariwala, D. X. Wu, Y. J. Li, A. Srivastava, Z. F. Wang, K. Storr, L. Balicas, F. Liu and P. M. Ajayan, *Nat. Mater.*, 2010, **9**, 430-435.
41 J. Kang, S. Tongay, J. B. Li and J. Q. Wu, *J. Appl. Phys.*, 2013, **113**, 143703.
42 C. H. Ho, C. S. Wu, Y. S. Huang, P. C. Liao and K. K. Tiong, *J. Phys.-Condens. Mat.*, 1998, **10**, 9317-9328.
43 S. M. Delphine, M. Jayachandran and C. Sanjeeviraja, *Crystallogr. Rev.*, 2011, **17**, 281-301.
44 Y. Aiura, I. Hase, K. Yagi-Watanabe, H. Bando, K. Ozawa, K. Tanaka, R. Kitagawa, S. Maruyama, T. Iwase, Y. Nishihara, K. Horiba, O. Shiino, M. Oshima, M. Nakatake, M. Kubota and K. Ono, *Phys. Rev. B*, 2004, **69**, 245123.
45 M. Moustafa, T. Zandt, C. Janowitz and R. Manzke, *Phys. Rev. B*, 2009, **80**, 035206.
46 C. Gaiser, T. Zandt, A. Krapf, R. Serverin, C. Janowitz and R. Manzke, *Phys. Rev. B*, 2004, **69**, 075205.

47 C. H. Ho, Y. S. Huang, P. C. Liao and K. K. Tiong, *Phys. Rev. B*, 1998, **58**, 12575-12578.
48 L. Y. Gan, Q. Y. Zhang, Y. J. Zhao, Y. C. Cheng and U. Schwingenschlog, *Sci. Rep.*, 2014, **4**, 6691.
49 J. Mann, Q. Ma, P. M. Odenthal, M. Isarraraz, D. Le, E. Preciado, D. Barroso, K. Yamaguchi, G. V. Palacio, A. Nguyen, T. Tran, M. Wurch, A. Nguyen, V. Klee, S. Bobek, D. Z. Sun, T. F. Heinz, T. S. Rahman, R. Kawakami and L. Bartels, *Adv. Mater.*, 2014, **26**, 1399-1404.
50 Y. J. Gong, Z. Liu, A. R. Lupini, G. Shi, J. H. Lin, S. Najmaei, Z. Lin, A. L. Elias, A. Berkdemir, G. You, H. Terrones, M. Terrones, R. Vajtai, S. T. Pantelides, S. J. Pennycook, J. Lou, W. Zhou and P. M. Ajayan, *Nano Lett.*, 2014, **14**, 442-449.
51 H. L. Li, X. D. Duan, X. P. Wu, X. J. Zhuang, H. Zhou, Q. L. Zhang, X. L. Zhu, W. Hu, P. Y. Ren, P. F. Guo, L. Ma, X. P. Fan, X. X. Wang, J. Y. Xu, A. L. Pan and X. F. Duan, *J. Am. Chem. Soc.*, 2014, **136**, 3756-3759.
52 Q. L. Feng, N. N. Mao, J. X. Wu, H. Xu, C. M. Wang, J. Zhang and L. M. Xie, *ACS Nano*, 2015, DOI: 10.1021/acsnano.1025b02506.
53 Q. L. Feng, Y. M. Zhu, J. H. Hong, M. Zhang, W. J. Duan, N. N. Mao, J. X. Wu, H. Xu, F. L. Dong, F. Lin, C. H. Jin, C. M. Wang, J. Zhang and L. M. Xie, *Adv. Mater.*, 2014, **26**, 2648-2653.
54 L. Yang, Q. Fu, W. H. Wang, J. Huang, J. L. Huang, J. Y. Zhang and B. Xiang, *Nanoscale*, 2015, **7**, 10490-10497.
55 Q. Fu, L. Yang, W. Wang, A. Han, J. Huang, P. Du, Z. Fan, J. Zhang and B. Xiang, *Adv. Mater.*, 2015, **27**, 4732-4738.
56 H. F. Liu, K. K. A. Antwi, S. Chua and D. Z. Chi, *Nanoscale*, 2014, **6**, 624-629.
57 J.-G. Song, G. H. Ryu, S. J. Lee, S. Sim, C. W. Lee, T. Choi, H. Jung, Y. Kim, Z. Lee, J.-M. Myoung, C. Dussarrat, C. Lansalot-Matras, J. Park, H. Choi and H. Kim, *Nat. Commun.*, 2015, **6**, 7817.
58 S. Tongay, D. S. Narang, J. Kang, W. Fan, C. H. Ko, A. V. Luce, K. X. Wang, J. Suh, K. D. Patel, V. M. Pathak, J. B. Li and J. Q. Wu, *Appl. Phys. Lett.*, 2014, **104**, 012101.
59 P. Schmidt, M. Binnewies, R. Glaum and M. Schmidt, in *Advanced Topics on Crystal Growth*, ed. S. O. Ferreira, InTech, 2013, ch. 9.
60 H. L. Li, Q. L. Zhang, X. D. Duan, X. P. Wu, X. P. Fan, X. L. Zhu, X. J. Zhuang, W. Hu, H. Zhou, A. L. Pan and X. F. Duan, *J. Am. Chem. Soc.*, 2015, **137**, 5284-5287.
61 X. S. Wang, H. B. Feng, Y. M. Wu and L. Y. Jiao, *J. Am. Chem. Soc.*, 2013, **135**, 5304-5307.
62 Y. J. Zhan, Z. Liu, S. Najmaei, P. M. Ajayan and J. Lou, *Small*, 2012, **8**, 966-971.
63 M. Zhang, Y. Zhu, X. Wang, Q. Feng, S. Qiao, W. Wen, Y. Chen, M. Cui, J. Zhang, C. Cai and L. Xie, *J. Am. Chem. Soc.*, 2015, **137**, 7051-7054.
64 S. H. Su, Y. T. Hsu, Y. H. Chang, M. H. Chiu, C. L. Hsu, W. T. Hsu, W. H. Chang, J. H. He and L. J. Li, *Small*, 2014, **10**, 2589-2594.
65 Q. Ma, M. Isarraraz, C. S. Wang, E. Preciado, V. Klee, S. Bobek, K. Yamaguchi, E. Li, P. M. Odenthal, A. Nguyen, D. Barroso, D. Z. Sun, G. V. Palacio, M. Gomez, A. Nguyen, D. Le, G. Pawin, J. Mann, T. F. Heinz, T. S. Rahman and L. Bartels, *ACS Nano*, 2014, **8**, 4672-4677.
66 O. L. Krivanek, M. F. Chisholm, V. Nicolosi, T. J. Pennycook, G. J. Corbin, N. Dellby, M. F. Murfitt, C. S. Own, Z. S. Szilagyi, M. P. Oxley, S. T. Pantelides and S. J. Pennycook, *Nature*, 2010, **464**, 571-574.
67 D. O. Dumcenco, H. Kobayashi, Z. Liu, Y. S. Huang and K. Suenaga, *Nat. Commun.*, 2013, **4**.
68 N. Tit, I. M. Obaidat and H. Alawadhi, *J. Phys.-Condens. Mat.*, 2009, **21**, 075802.
69 H. P. Komsa and A. V. Krasheninnikov, *J. Phys. Chem. Lett.*, 2012, **3**, 3652-3656.
70 L. Genzel, T. P. Martin and C. H. Perry, *Phys. Status Solidi B*, 1974, **62**, 83-92.
71 S. Rath, M. L. Hsieh, P. Etchegoin and R. A. Stradling, *Semicond. Sci. Technol.*, 2003, **18**, 566-575.
72 P. Parayanthal and F. H. Pollak, *Phys. Rev. Lett.*, 1984, **52**, 1822-1825.
73 Y. F. Chen, D. O. Dumcenco, Y. M. Zhu, X. Zhang, N. N. Mao, Q. L. Feng, M. Zhang, J. Zhang, P.-H. Tan, Y.-S. Huang and L. M. Xie, *Nanoscale*, 2013, **6**, 2833-2839.
74 I. F. Chang and S. S. Mitra, *Phys. Rev.*, 1968, **172**, 924-933.
75 J. Jadczak, D. O. Dumcenco, Y. S. Huang, Y. C. Lin, K. Suenaga, P. H. Wu, H. P. Hsu and K. K. Tiong, *J. Appl. Phys.*, 2014, **116**, 193505.
76 J. Y. Xi, T. Q. Zhao, D. Wang and Z. G. Shuai, *J. Phys. Chem. Lett.*, 2014, **5**, 285-291.
77 Y. H. Lee, L. L. Yu, H. Wang, W. J. Fang, X. Ling, Y. M. Shi, C. T. Lin, J. K. Huang, M. T. Chang, C. S. Chang, M. Dresselhaus, T. Palacios, L. J. Li and J. Kong, *Nano Lett.*, 2013, **13**, 1852-1857.
78 V. Klee, E. Preciado, D. Barroso, A. E. Nguyen, C. Lee, K. J. Erickson, M. Triplett, B. Davis, I. H. Lu, S. Bobek, J. McKinley, J. P. Martinez, J. Mann, A. A. Talin, L. Bartels and F. Leonard, *Nano Lett.*, 2015, **15**, 2612-2619.
79 T. F. Jaramillo, K. P. Jorgensen, J. Bonde, J. H. Nielsen, S. Horch and I. Chorkendorff, *Science*, 2007, **317**, 100-102.
80 Q. F. Gong, L. Cheng, C. H. Liu, M. Zhang, Q. L. Feng, H. L. Ye, M. Zeng, L. M. Xie, Z. Liu and Y. G. Li, *ACS Catal.*, 2015, **5**, 2213-2219.
81 V. Kiran, D. Mukherjee, R. N. Jenjeti and S. Sampath, *Nanoscale*, 2014, **6**, 12856-12863.
82 B. Liu, M. Köpf, A. N. Abbas, X. Wang, Q. Guo, Y. Jia, F. Xia, R. Weihrich, F. Bachhuber, F. Pielnhofer, H. Wang, R. Dhall, S. B. Cronin, M. Ge, X. Fang, T. Nilges and C. Zhou, *Adv. Mater.*, 2015, **27**, 4423-4429.